Electronic Supplementary File

Construction of g-C_3N_4/PANI/α-MnO_2 Direct Z-scheme Heterojunction with Oxygen-Rich Vacancies Enhanced Photocatalytic Degradation of Tetracycline Hydrochloride under Visible light

Nisar Ahmad Chopan[1] and Hamida-Tun-Nisa Chishti[1*]

Department of Chemistry, National Institute of Technology, Srinagar, 190006, India

X-ray photoelectron spectroscopy (XPS) of pristine g-C_3N_4, α-MnO_2, PANI, and 20-G/0.5-P/M composite.

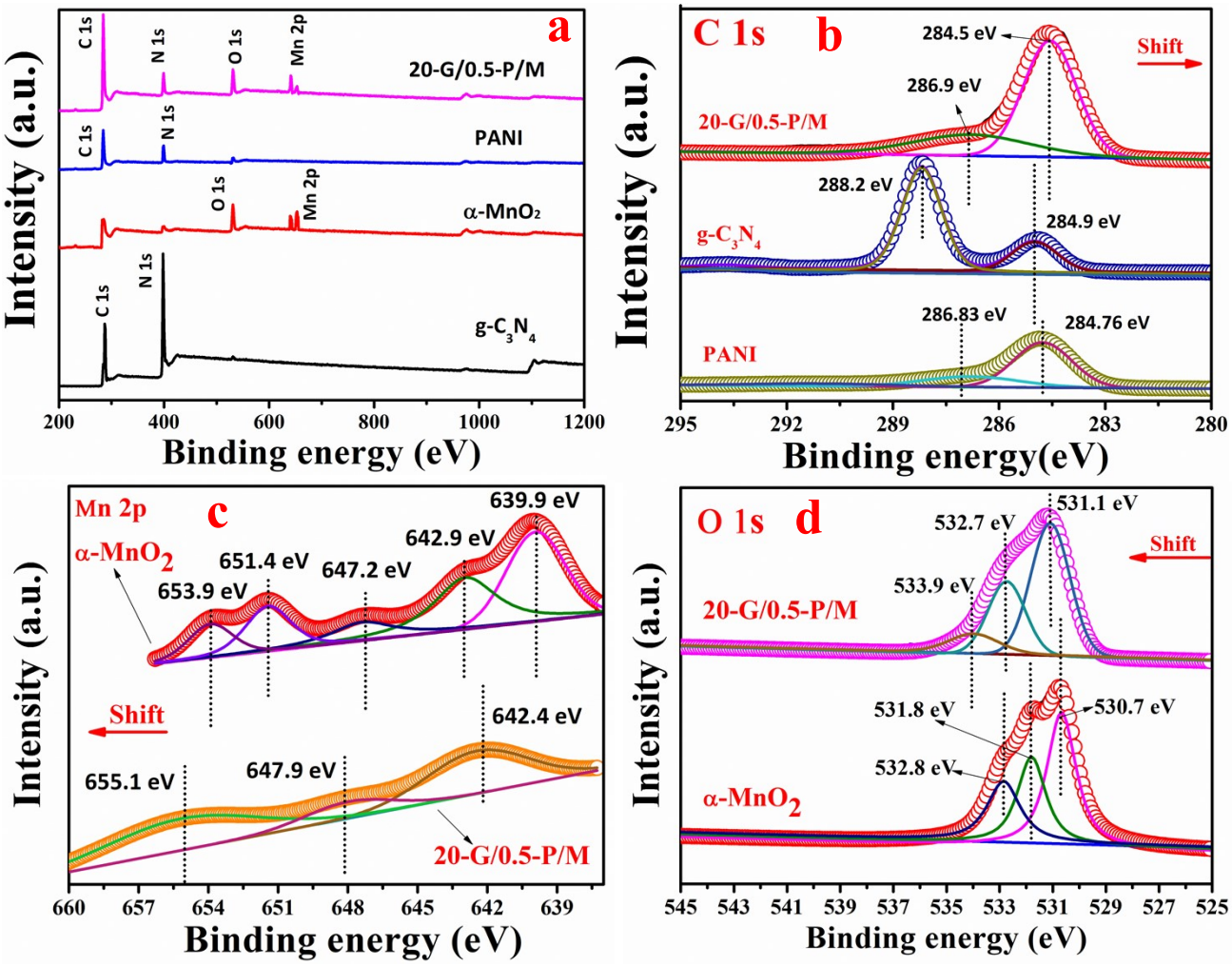

Fig. S1 XPS of (a) survey spectrum of pristine g-C_3N_4, α-MnO_2, PANI, and 20-G/0.5-P/M composite, (b) C 1s of pristine g-C_3N_4, PANI, and 20-G/0.5-P/M composite, (c) Mn 2p of pristine α-MnO_2, and 20-G/0.5-P/M composite, and (d) O 1s of pristine α-MnO_2, and 20-G/0.5-P/M composite.

Electron Paramagnetic spectroscopy (EPR):

The electron spin resonance (ESR) test is further employed to explore whether the semiconductors g-C_3N_4, α-MnO_2, and composite 20-G/0.5-P/M are ESR active or not (i.e., to know whether these materials possess reactive species like hydroxide radicle, superoxide radicle, and free electron). As depicted in Fig. S2 (a, b, c) there occurs peaks in the ESR spectrum of these materials under light only, which confirms that these materials are ESR active and will be involved in the degradation of the TC antibiotic as already explained in Fig. 11d. The intensity of peaks in light, of these materials increases in the following order, α-MnO_2 < g-C_3N_4< 20-G/0.5-P/M, which indicates that 20-G/0.5-P/M composite is the most ESR active out of the three materials mentioned above.

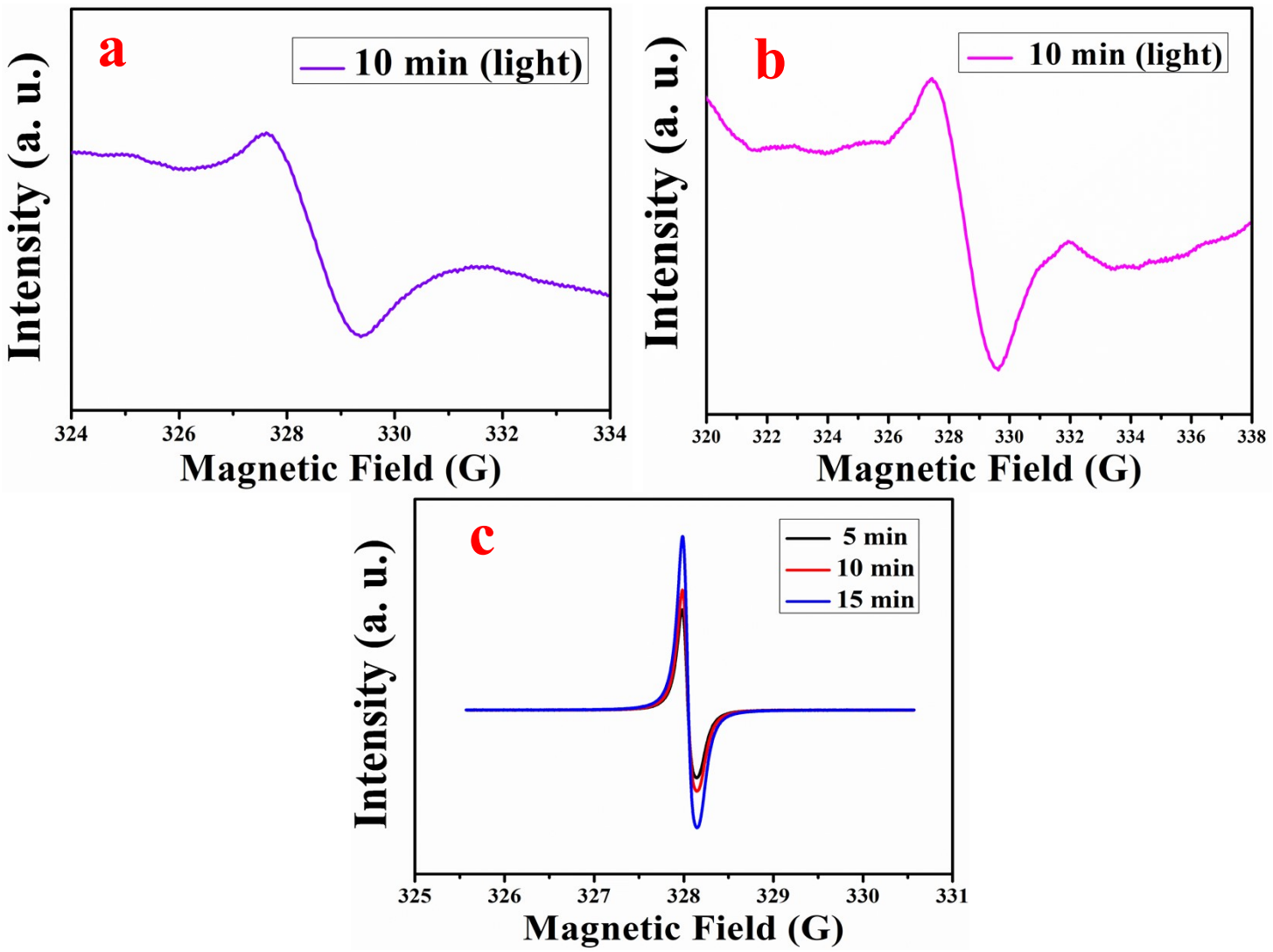

Fig. S2 ESR spectra of (a) α-MnO_2, (b) g-C_3N_4, and (c) 20-G/0.5-P/M catalysts in presence of light.

TA Experiments.

Terephthalic acid (TA) experiments were conducted in order to find out the formation of hydroxyl radicals in the reaction mixture. Generally, TA reacts with generated •OH radicals to form 2-hydroxyterephthalic acid complex (TAOH) and formation of this complex can be encountered at λ= 429 nm [1]. In the given Fig. S3, an intense peak is observed at λ= 429 which confirms the formation and generation of •OH radicals and supports the degradation process. As shown in Fig. S3, it is obvious that the amount of hydroxyl radicals produced by each photocatalyst increased with increasing irradiation time as shown in the PL intensity [2]. It was found that the amount of hydroxyl radicals generated by α-MnO_2 was lower than that of g-C_3N_4 photocatalyst synthesized in this study. Furthermore, the concentration of hydroxyl radical produced by 20-G/0.5-P/M nanocomposites was significantly greater than that of individual photocatalysts i.e., α-MnO_2, and g-C_3N_4 due to the simultaneous trapping of the generated electrons from the valence and conduction bands by the two dopants. The order of concentration of hydroxyl radicals formed during photocatalysis was 20-G/0.5-P/M > 20-G/M > g-C_3N_4> α-MnO_2 photocatalysts. The observed activity and OH radicals may be ascribed to the presence of visible radiation. This further corroborates the results of the photocatalytic performance shown in Figs. S4 and revealed that the amount of surface bound OH radicals formed is the function of the synthesized material. The differences in the concentration of hydroxyl radicals produced by each sample may be linked to specific surface areas, band gap, and the radiation time.

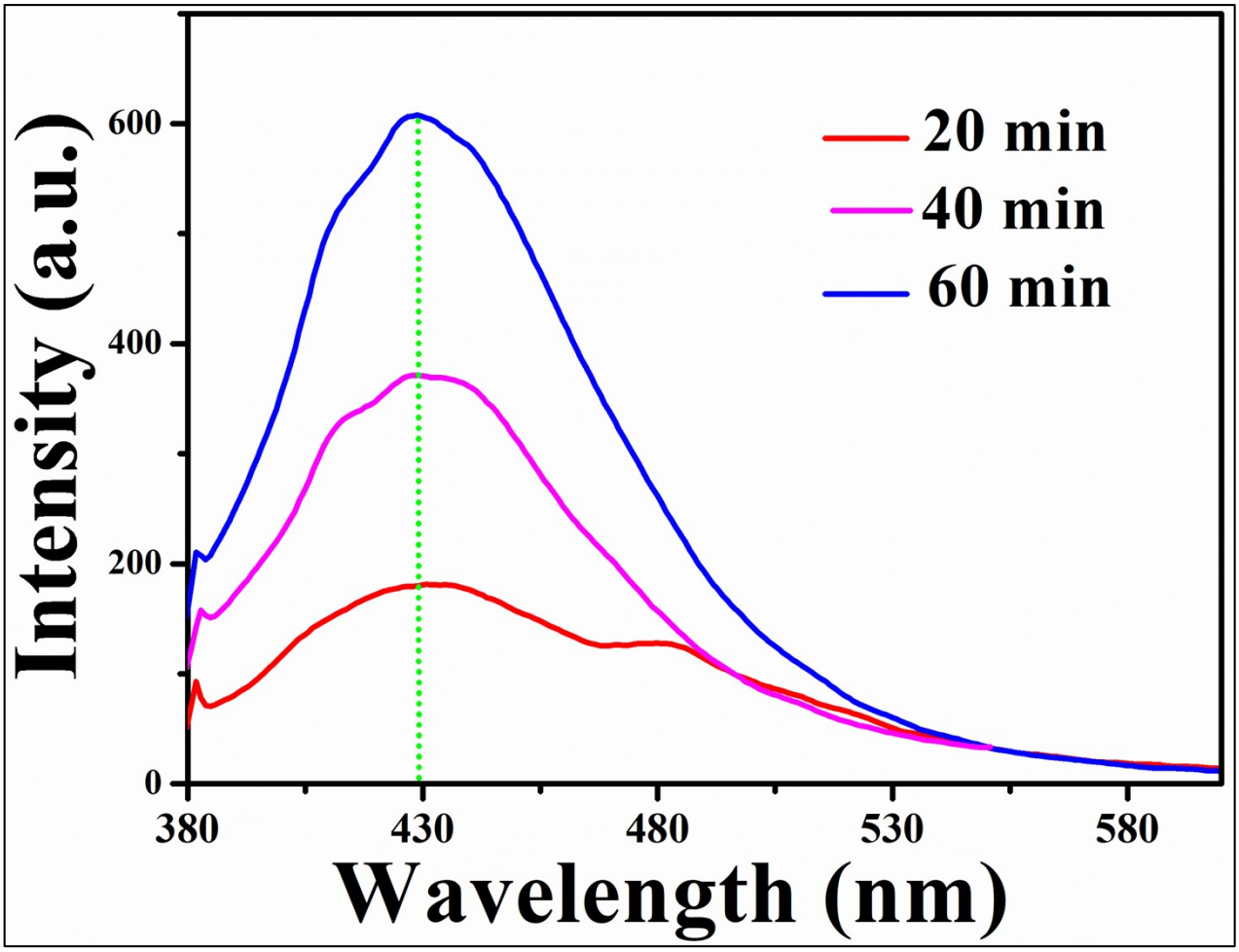

Fig. S3 PL spectra observed using 20-G/M/0.5-P nanocomposites at different time intervals.

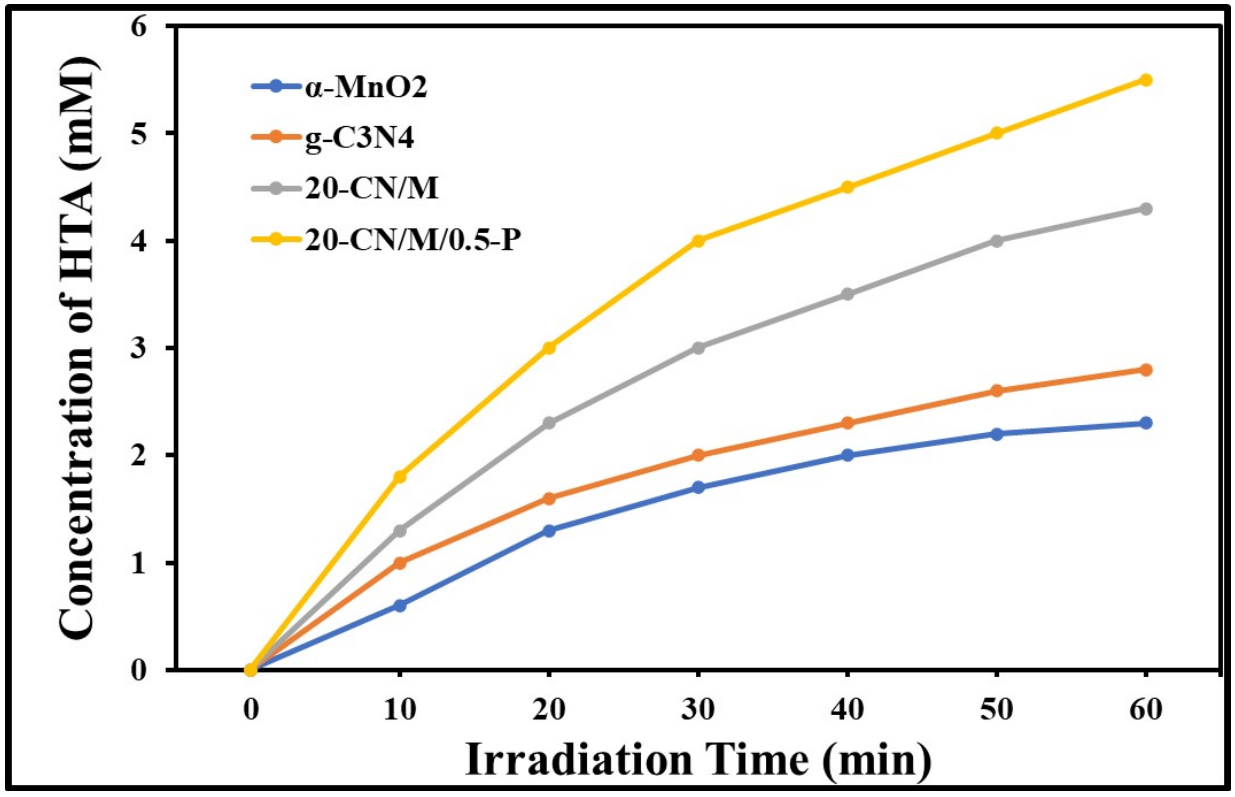

Fig. S4 Concentration of HTA by various photocatalysts upon irradiation of visible light.

Photocatalytic stability and durability of the catalyst:

The stability of the catalyst was confirmed by XRD, FTIR, XPS, FESEM and TEM characterization techniques after five consecutive cycles were conducted to further evidence the higher stability of the composites. In Figures S5, S6, S7, S8, and S9, no obvious changes in morphology or structure of used 20-G/0.5-P/M were observed. In Fig. S5, it could be seen that the characteristic diffraction peaks of 20-G/0.5-P/M still maintained in the XRD patterns of used sample and no additional diffraction peaks were observed. In Fig. S6, there occurs no change in the FTIR spectra of the 20-G/0.5-P/M composite even after the five consecutive cycles of photodegradation of TC antibiotics. In Fig. S7, the peaks of Mn 2p, C 1s, N 1s and O 1s were detected in the XPS spectrum of used 20-G/0.5-P/M composite and appears without any alteration and no any additional peak was observed. In Fig. S8 and Fig S9, in which there were no obvious changes in the morphology as displayed by the FESEM and TEM images of the used

samples, strongly verifying the higher stability of 20-G/0.5-P/M composite during the photocatalytic process.

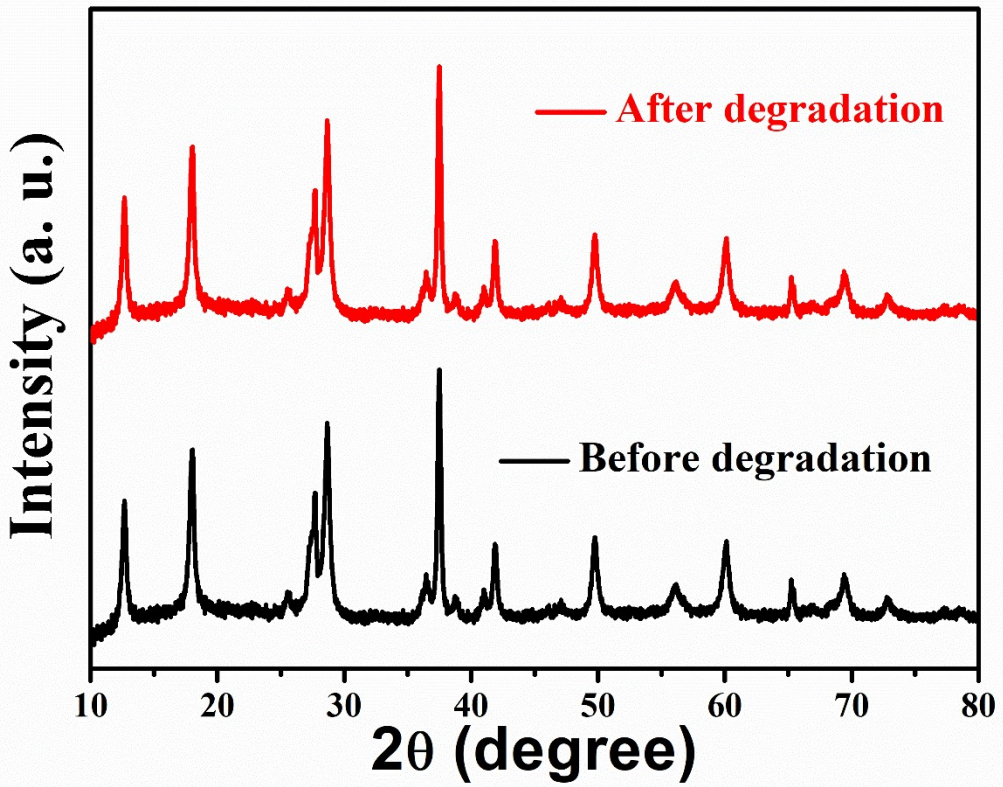

Fig. S5 XRD of 20-G/0.-P/M before and after photodegradation of TC.

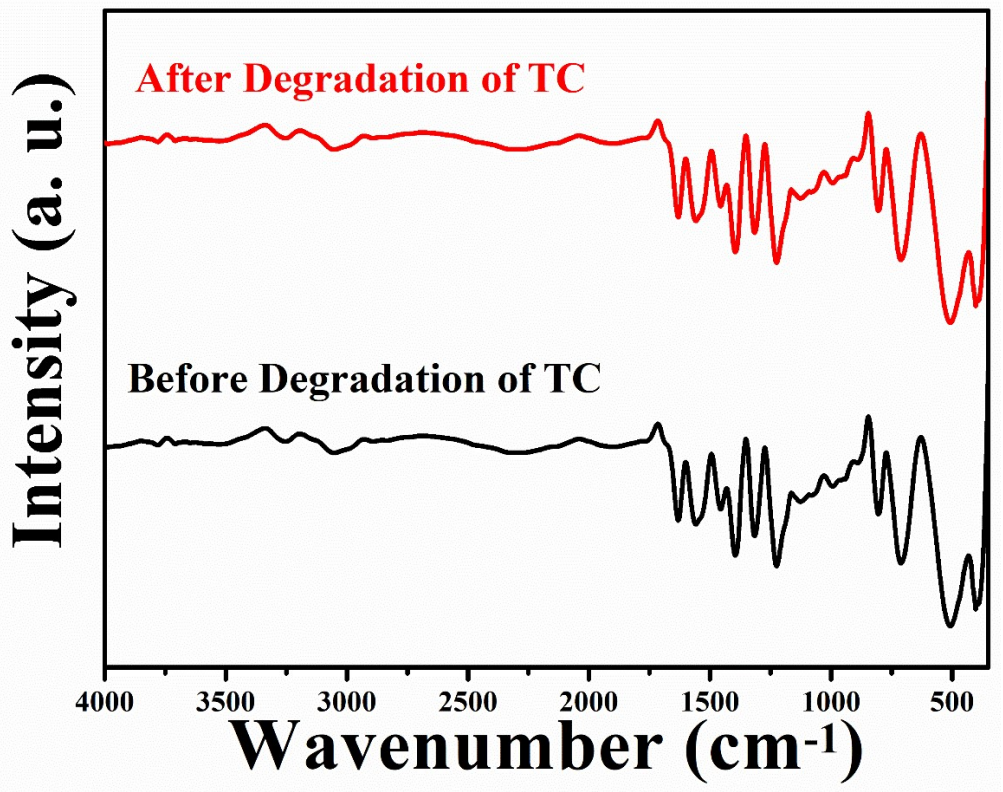

Fig. S6 FTIR of 20-G/0.-P/M catalyst before and after photodegradation of TC.

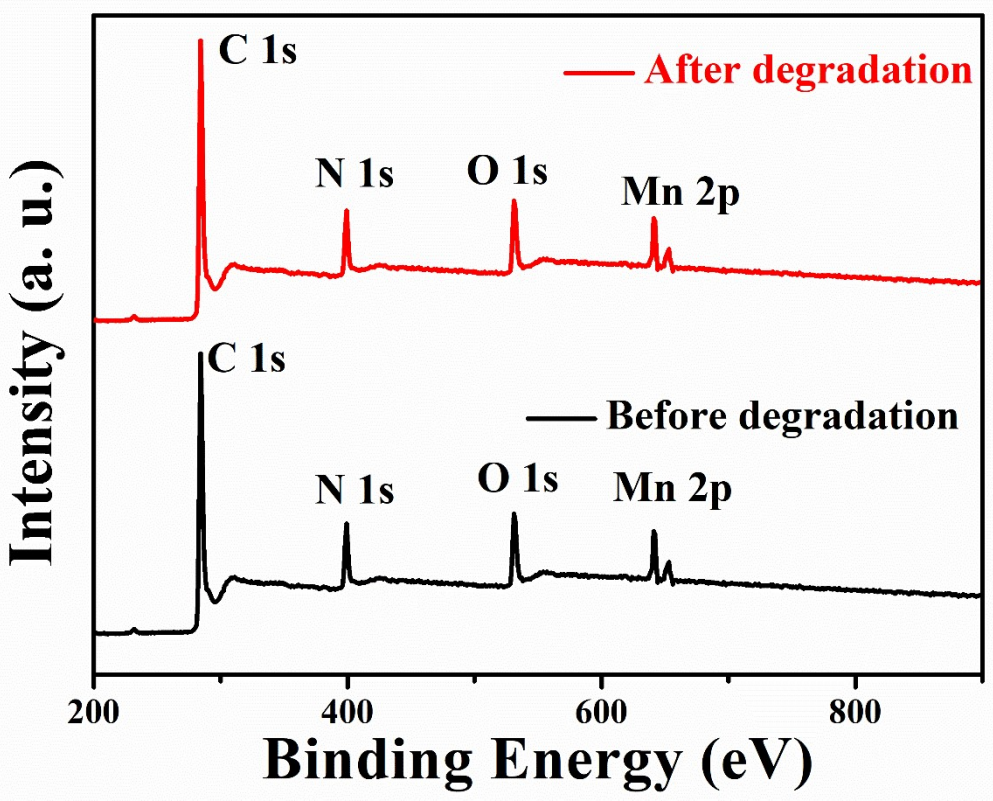

Fig. S7 XPS of 20-G/0.-P/M catalyst before and after photodegradation of TC.

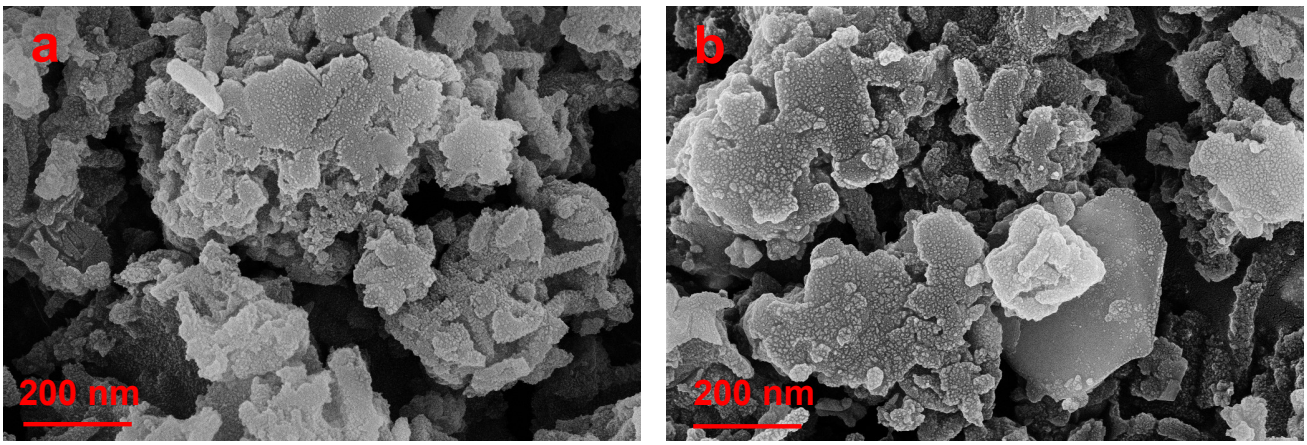

Fig. S8 FESEM of 20-G/0.-P/M catalyst before and after photodegradation of TC.

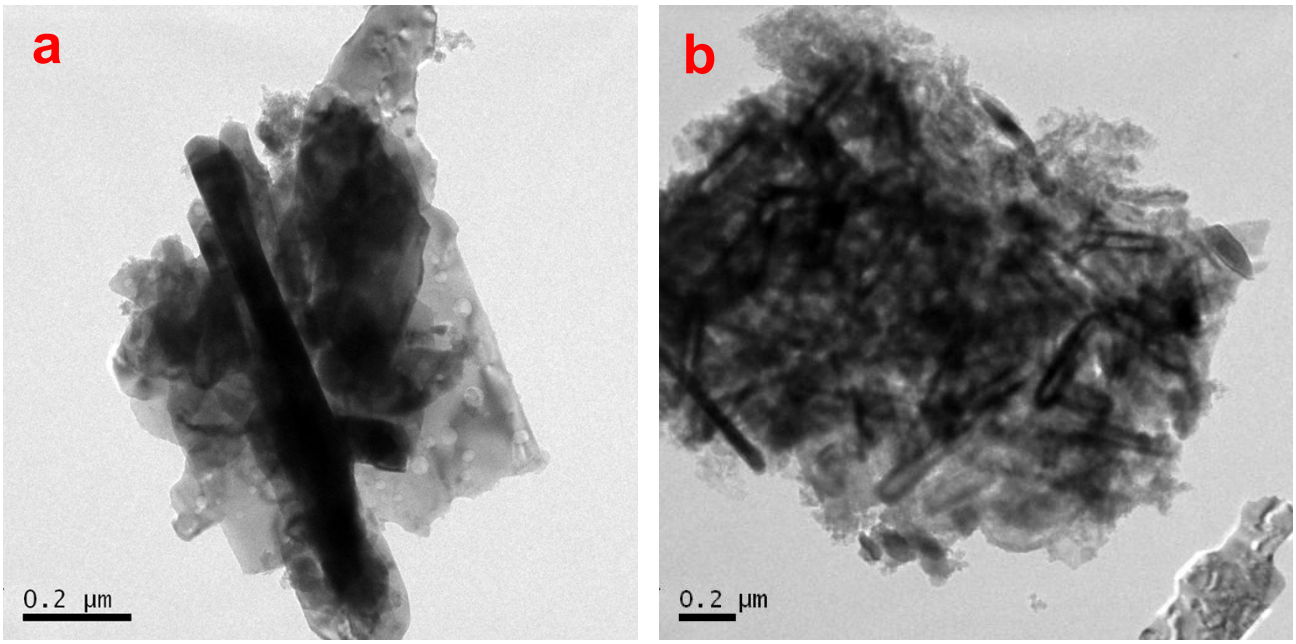

Fig. S9 TEM of 20-G/0.-P/M catalyst before and after photodegradation of TC.

Mineralization of the TC antibiotic:

The mechanism of decomposition of organic pollutants in the antibiotic wastewater by α-MnO_2-based photocatalysts usually follows three main pathways such as transfer of pollutant from the liquid bulk to the catalyst surface, followed by adsorption of organic pollutants onto the surface of the catalyst, in this case 20-G/0.5-P/M nanocomposite and lastly photodegradation of organic pollutants by the catalyst. The degree of mineralization of antibiotics in the wastewater by the present photocatalyst as a function of reaction time is expressed in the form of TOC [3–5]. The % TOC removal by the action of the 20-G/0.5-P/M with respect to irradiation time. For instance, in Fig. S10, the TOC removal was approximately 96% under artificial visible light irradiation after 60 min. This implies that the photocatalytic degradation of TC achieved the desired mineralization effect. The reason of enhanced photocatalytic behaviour of the nanocomposites may be linked to the nature of the pollutants, duration of the reaction, surface area, and the band gap energy.

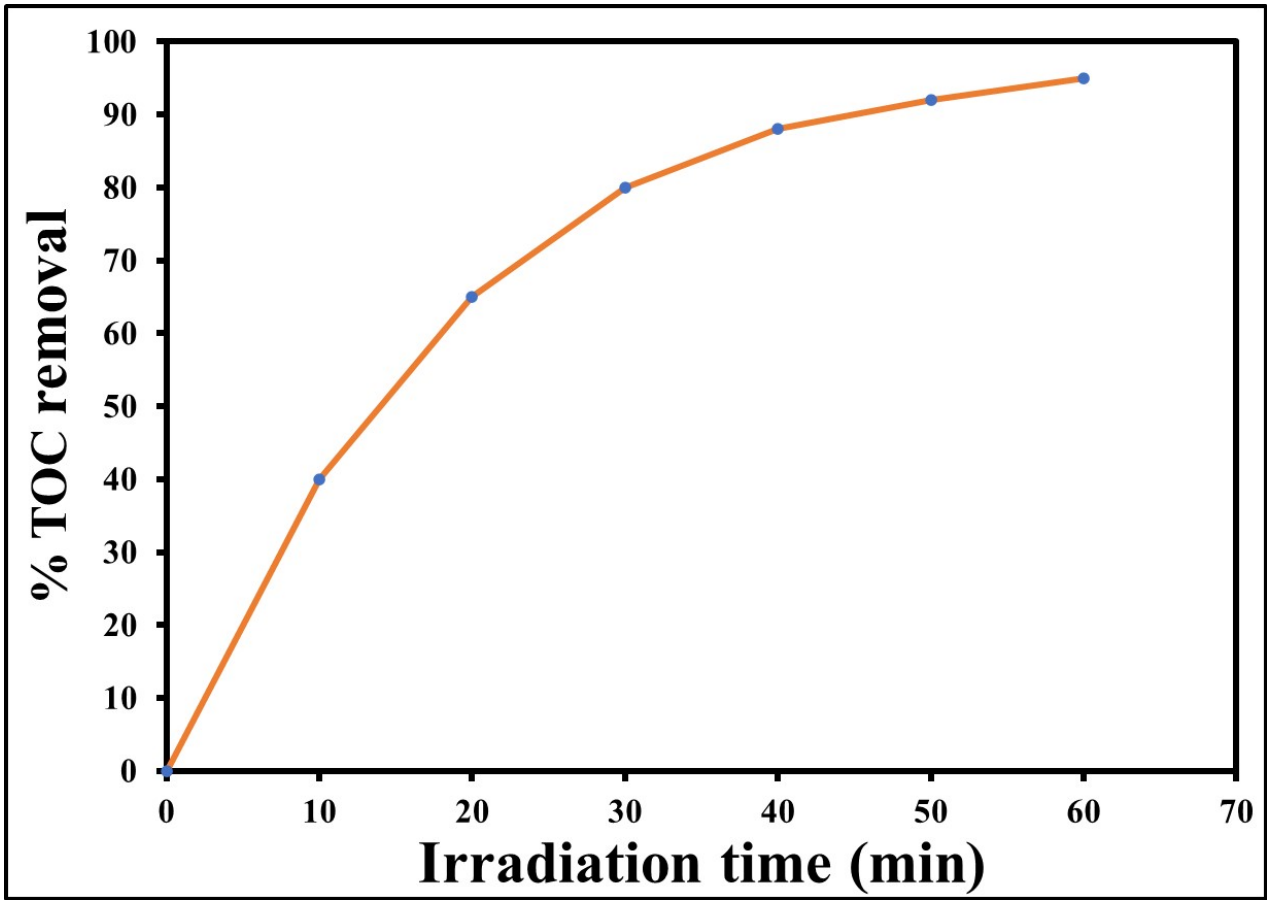

Fig. S10 TOC removal from the local antibiotic wastewater under visible light (experimental conditions: 50 mg/1 cm^3, 60 min, 150 rpm, visible light intensity 125 W).

References:

[1] Y.-Y. Yang, H.-P. Feng, C.-G. Niu, D.-W. Huang, H. Guo, C. Liang, H.-Y. Liu, S. Chen, N. Tang, L. Li, Constructing a plasma-based Schottky heterojunction for near-infrared-driven photothermal synergistic water disinfection: Synergetic effects and antibacterial mechanisms, Chem. Eng. J. 426 (2021) 131902. https://doi.org/10.1016/j.cej.2021.131902.

[2] Y.-Y. Yang, X.-G. Zhang, C.-G. Niu, H.-P. Feng, P.-Z. Qin, H. Guo, C. Liang, L. Zhang, H.-Y. Liu, L. Li, Dual-channel charges transfer strategy with synergistic effect of Z-scheme heterojunction and LSPR effect for enhanced quasi-full-spectrum photocatalytic bacterial inactivation: new insight into interfacial charge transfer and molecular oxygen activation, Appl. Catal. B Environ. 264 (2020) 118465. https://doi.org/10.1016/j.apcatb.2019.118465.

[3] S.K. and E.P., Biogenic synthesis of ZnO-Ag nano custard apples for efficient photocatalytic degradation of methylene blue by sunlight irradiation, (n.d.).

[4] J.O. Tijani, U.O. Momoh, R.B. Salau, M.T. Bankole, A.S. Abdulkareem, W.D. Roos, Synthesis and characterization of Ag2O/B2O3/TiO2 ternary nanocomposites for photocatalytic mineralization of local dyeing wastewater under artificial and natural sunlight irradiation, Environ. Sci. Pollut. Res. 26 (2019) 19942–19967. https://doi.org/10.1007/s11356-019-05124-y.

[5] D. Toloman, A. Popa, M. Stan, M. Stefan, G. Vlad, S. Ulinici, G. Baisan, T.D. Silipas, S. Macavei, C. Leostean, S. Pruneanu, F. Pogacean, R.C. Suciu, L. Barbu-Tudoran, O. Pana, Visible-light-driven photocatalytic degradation of different organic pollutants using Cu doped ZnO-MWCNT nanocomposites, J. Alloys Compd. 866 (2021) 159010. https://doi.org/10.1016/j.jallcom.2021.159010.